GENEAR: AUTOREGRESSIVE GENE-TO-WSI TILE SYNTHESIS VIA CAUSAL MEANFLOW

Anonymous authors
Paper under double-blind review

ABSTRACT

Understanding how transcriptomic programs shape tissue morphology remains a central challenge in computational pathology. Gene-to-WSI tile synthesis offers a principled generative framework to translate molecular profiles into histological images. However, most existing methods compress RNA-Seq into a single global embedding injected once at initialization, an oversimplified design that weakens transcriptomic signals and induces non-causal associations between gene expression and tissue morphology. We present GeneAR, an Autoregressive Gene-to-WSI model that reformulates synthesis as an iterative, coarse-to-fine generative process. At its core is a novel Causal MeanFlow module that reinforces transcriptome-informed guidance at multiple stages and mitigates non-causal factors through counterfactual-style interventions, thereby ensuring biological fidelity throughout the generative trajectory. Combined with a β-VAE for compact gene embeddings and a multi-scale vector quantizer for discrete morphology representation, GeneAR generates H&E-stained WSI tiles that are both visually realistic and transcriptomically faithful. Extensive experiments across five TCGA cancer benchmarks demonstrate consistent state-of-the-art performance, surpassing prior methods in both generative fidelity and downstream classification accuracy. All models and code will be released to facilitate reproducibility.

1 INTRODUCTION

A central question in computational pathology is how transcriptomic programs shape tissue morphology, and whether pathology images can be generated directly from RNA-Seq to probe this link (Coudray et al., 2018; Schmauch et al., 2020). Framing this as *Gene-to-WSI tile synthesis* is both scientifically meaningful and practically useful: it enables in silico experiments on how molecular perturbations manifest morphologically, provides privacy-preserving synthetic data for model development, and improves label/data efficiency in downstream tasks such as cancer classification or biomarker discovery (Ktena et al., 2024; Chang et al., 2023). Beyond augmentation, Gene–to–WSI generation offers a controlled testbed for multi-omics hypothesis generation and can boost statistical power where real images or labels are scarce or imbalanced (Chen et al., 2025).

Despite its promise, Gene-to-WSI tile synthesis remains methodologically underdeveloped. Existing solutions typically compress RNA-Seq profiles into low-dimensional embeddings that either drive one-shot generators (e.g., GAN variants) (Carrillo-Perez et al., 2023) or condition cascaded diffusion pipelines (Carrillo-Perez et al., 2025). While feasible, these strategies face structural limitations that undermine biological fidelity and scalability. First, collapsing the transcriptome into a static embedding injected only once causes *signal decay*, with molecular guidance fading as generation unfolds and images drifting toward superficial correlations rather than gene-driven morphology. Second, synthesizing tiles at a fixed resolution introduces *scale rigidity*,

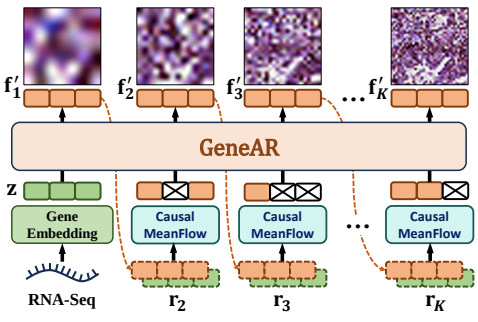

Figure 1: **Key Idea.** GeneAR integrates Causal MeanFlow into an autoregressive framework, where transcriptomic guidance is iteratively injected with causal enhancement to ensure biologically faithful WSI synthesis.

weakening cross-scale semantic consistency and diminishing transcriptome–morphology alignment. Third, embeddings are learned in a purely correlational manner, leaving models vulnerable to *confounders* such as batch effects, tumor purity, and staining variability, thereby undermining causal fidelity.

To address these challenges, we reformulate Gene-to-WSI synthesis as an *iterative, coarse-to-fine generative process* in which transcriptomic signals are injected at multiple stages during generation rather than used once at initialization. Building on this principle, we propose GeneAR—the first autoregressive Gene-to-WSI model that delivers stepwise molecular reinforcement while preserving structural coherence and causal fidelity (see Fig. 1). While drawing inspiration from recent advances in visual autoregression (Tian et al., 2024), GeneAR extends this paradigm into the molecular domain by conditioning coarse-to-fine prediction on compact, biologically grounded embeddings derived from a β-VAE. This integration ensures that the transcriptome remains an active driver of morphology, enabling dynamic cross-scale guidance during decoding. As a result, GeneAR prevents *signal decay*, enforces *multi-scale consistency*, and strengthens the causal alignment between gene programs and emergent tissue organization.

Yet an iterative paradigm alone does not immunize the generative trajectory against *confounders*—such as batch effects, tumor purity, and staining variability—whose correlational footprints can divert decoding from gene-driven semantics (Leek et al., 2010; Aran et al., 2015). To address this, Causal MeanFlow is introduced as a gene-driven causal module intrinsically embedded in the autoregressive trajectory. Inspired by average velocity fields (Geng et al., 2025), it reformulates flow dynamics in a biological context by directly coupling generative updates with transcriptomic embeddings. During training, counterfactual interventions disentangle causal signals from spurious variation, while at inference the learned field governs generation independently without auxiliary samples. More than an auxiliary add-on, Causal MeanFlow functions as an integral mechanism that injects transcriptomic guidance at multiple stages, suppresses non-causal drift, and preserves structural coherence. Through this integration, GeneAR establishes a generative framework in which transcriptomic signals remain active, consistent, and causally faithful throughout synthesis.

We validate GeneAR on five TCGA benchmarks spanning diverse cancer types. Across all datasets, GeneAR attains the lowest Fréchet Inception Distance (FID), indicating superior generative fidelity, and achieves the highest accuracy and F1 score in downstream cancer classification. These results confirm that GeneAR not only synthesizes realistic morphology faithfully aligned with transcriptomic profiles, but also produces synthetic data that directly enhance predictive modeling. Our main **contributions** are summarized as follows:

- **Paradigm Shift.** GeneAR reformulates Gene-to-WSI synthesis as an *iterative, coarse-to-fine generative process* in which transcriptomic signals are injected at multiple stages across scales, overcoming the signal decay and rigidity of static global embeddings.
- **Causal Fidelity.** By integrating the novel Causal MeanFlow module into the autoregressive trajectory, GeneAR disentangles transcriptomic effects from confounders, ensuring that morphological synthesis remains biologically grounded and causally aligned.
- **State-of-the-Art Performance.** Comprehensive evaluation on five TCGA cohorts demonstrates that GeneAR attains the lowest FID and the highest accuracy in downstream classification, setting a new benchmark for both generative fidelity and functional utility.

2 Related Works

Gene-to-WSI Synthesis. In recent years, most prior studies in computational pathology focus on predicting gene expression from WSIs (Schmauch et al., 2020; Pizurica et al., 2024; Chung et al., 2024; Ganguly et al., 2025), whereas the inverse task—synthesizing histology directly from RNA-Seq—remains underexplored. Early attempts such as RNA-GAN (Carrillo-Perez et al., 2023) inject transcriptomic information only once and operate at a fixed resolution, while cascaded diffusion models (Carrillo-Perez et al., 2025) improve visual fidelity but still rely on static conditioning and fail to account for confounders. Motivated by these challenges, we propose a *multi-stage, coarse-to-fine Gene-to-WSI framework* that injects transcriptomic guidance throughout decoding, preventing signal decay, and explicitly disentangles causal signals from spurious variation, thereby enabling more robust and biologically faithful histology synthesis.

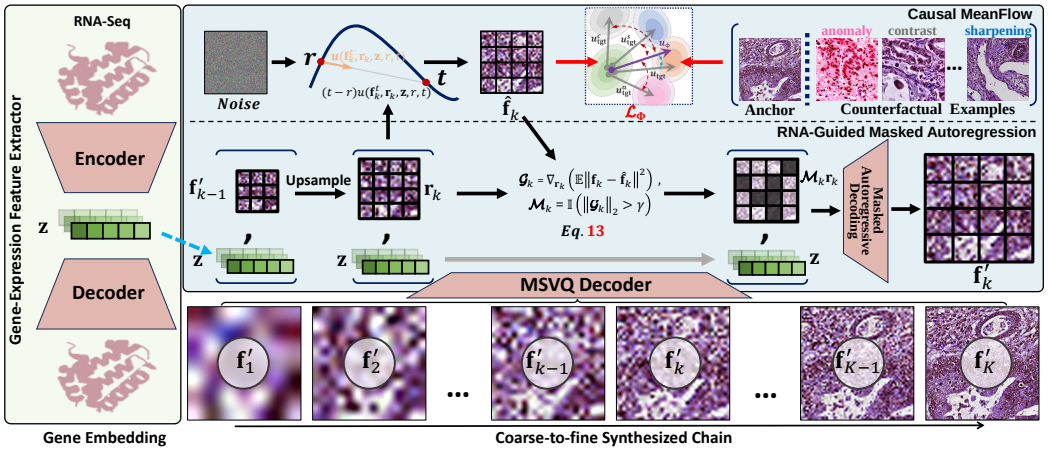

Figure 2: **Overview of GeneAR**. RNA-Seq embeddings are injected into a multi-scale autoregressive pipeline, where morphology is reconstructed from $\mathbf{f}_K^{'}$ via the MSVQ decoder and reinforced by Causal MeanFlow with counterfactual supervision (see Sec. 3 for details).

Autoregressive Image Generation. Autoregressive transformers have reframed image synthesis as sequential token modeling (Van Den Oord et al., 2017; Razavi et al., 2019; Chen et al., 2020; Esser et al., 2021), further extended through residual quantization (Lee et al., 2022a), iterative refinement (Chang et al., 2022; Lee et al., 2022b), and scalable codebooks (Yu et al., 2023). Coarse-to-fine autoregression (Tian et al., 2024) achieves diffusion-level quality at lower sampling cost. Despite these advances, applications in computational pathology remain absent, where Gene-to-WSI pipelines still rely on GANs or diffusion (Carrillo-Perez et al., 2023; 2025). Our study introduces the first multi-scale autoregressive framework for RNA-guided WSI tile generation that preserves transcriptomic guidance and cross-scale consistency.

Causal Generative Modeling. Gene-to-WSI methods remain vulnerable to confounders such as staining or tumor purity (Leek et al., 2010; Macenko et al., 2009; Aran et al., 2015), with normalization or domain adaptation providing only partial remedies. In contrast, causal generative modeling (Schölkopf et al., 2021; Wu et al., 2024; Gao et al., 2025) and flow-based dynamics (Geng et al., 2025) offer new approaches to disentangling causal signals and improving stability, yet these advances have not been applied in pathology. We introduce a Causal MeanFlow module that embeds causal constraints into autoregressive training, ensuring persistent gene-driven semantics and suppressing spurious correlations.

3 Methodology

3.1 Preliminaries

Reformulation. Recent studies show that transcriptomic programs are tightly coupled with tissue morphology and can even define layered cytoarchitectural organization in development (Schmauch et al., 2020; Qian et al., 2025). This suggests that Gene-to-WSI synthesis should preserve transcriptomic guidance dynamically across scales. However, existing methods collapse RNA-Seq into static embeddings injected once, leading to signal decay, scale rigidity, and spurious correlations. To overcome these issues, we reformulate Gene-to-WSI synthesis as a coarse-to-fine autoregressive process, where an image is quantized into hierarchical token maps $\mathcal{S} = \{s_k\}_{k=1}^{n}$ and generated sequentially under recurrent guidance from $\mathbf{g}$:

$$s_k = \mathcal{P}_\Theta(s_{<k}, \mathbf{g}). \tag{1}$$

Here, $\mathbf{g}$ is injected at multiple stages rather than only once at initialization, ensuring that transcriptomic signals remain persistently active throughout the generative trajectory while leveraging the distributional strength of autoregressive models (Esser et al., 2021; Lee et al., 2022a; Tian et al., 2024).

Multi-Scale Vector Quantization. We employ the multi-scale vector quantization (MSVQ) (Tian et al., 2024) to discretize a WSI tile $X \in \mathbb{R}^{H\times W\times C}$ into K hierarchical token maps $\mathcal{S} = \{s_k\}_{k=1}^{K}$,

where each $s_k \in \mathbb{R}^{h_k \times w_k}$ denotes a discrete map at scale k. Unlike single-token quantization, MSVQ outputs entire token maps, which reduces inference cost and preserves cross-scale structure. For autoregressive modeling, the final-scale map s_K is excluded, and the remaining maps are embedded by $\mathcal{W}$ and interpolated by $\mathcal{U}$, producing latent features $\mathcal{F} = \{\mathbf{f}_k\}_{k=1}^{K}$ and token embeddings $\mathcal{R} = \{\mathbf{r}_k\}_{k=2}^{K}$:

$$\mathbf{f}_k = \sum_{i=1}^{k} \mathcal{U}(\mathcal{W}(s_i), h_K \times w_K), \quad \mathbf{r}_{k+1} = \mathcal{U}(\mathbf{f}_k, h_{k+1} \times w_{k+1}), \tag{2}$$

where $\mathbf{f}_k \in \mathbb{R}^{h_K \times w_K \times d}$ aggregates multi-scale information up to level k, and $\mathbf{r}_{k+1} \in \mathbb{R}^{h_{k+1} \times w_{k+1} \times d}$ provides scale-aligned embeddings.

During decoding, similar to (Li et al., 2024b), the MSVQ decoder progressively reconstructs the tissue tile from $\mathbf{f}_K$ by residual refinement across scales, combining quantized maps and convolutional upsampling to recover both semantic structure and fine-grained details.

3.2 Autoregressive Gene-to-WSI Tile Modeling

We propose GeneAR, which reformulates gene-conditioned pathology synthesis as an *iterative, coarse-to-fine generative process*. As shown in Fig. 2, GeneAR incorporates transcriptomic signals through three key components: **(1)** *Gene-Expression Feature Extractor*, which encodes RNA-Seq profiles $\mathbf{g} \in \mathbb{R}^{17655}$ into a compact latent prior $\mathbf{z} \in \mathbb{R}^{200}$; **(2)** *Causal MeanFlow*, which refines scale-wise responses $\mathbf{r}_k$ into causality-enhanced features $\hat{\mathbf{f}}_k$ under the guidance of $\mathbf{z}$; **(3)** *RNA-guided Masked Autoregression*, which constructs masks $\mathcal{M}_k$ from discrepancies between $\hat{\mathbf{f}}_k$ and $\mathbf{f}_k$ to highlight transcriptomic cues, and concatenates $\mathbf{z}$ with $\{\mathcal{M}_k \mathbf{r}_k\}_{k=2}^{K}$ for autoregressive decoding into the reconstructed token maps $\hat{\mathcal{S}} = \{\mathbf{s}_k^{'}\}_{k=1}^{K}$, together with features $\hat{\mathcal{F}} = \{\mathbf{f}_k^{'}\}_{k=1}^{K}$.

Gene-Expression Feature Extractor. Transcriptomic (RNA-Seq) profiles are inherently high-dimensional, necessitating compact yet biologically meaningful representations for effective integration into generative models. Following RNA-CDM (Carrillo-Perez et al., 2025), we adopt a β-VAE (Higgins et al., 2017) with a two-layer encoder f_ψ and decoder g_θ. Each RNA-Seq profile $\mathbf{g}$ is projected into a latent code $\mathbf{z}$, from which a reconstruction $\mathbf{g}'$ is generated. The training objective is

$$\mathcal{L}_{\psi,\theta} = -\mathbb{E}_{f_\psi(\mathbf{z}|\mathbf{g})}[log(g_\theta(\mathbf{g}|\mathbf{z}))] + \beta \cdot \mathbb{KL}(f_\psi(\mathbf{z}|\mathbf{g})||p(\mathbf{z})), \tag{3}$$

with β regulating the trade-off between reconstruction fidelity and latent regularization. The resulting $\mathbf{z}$ serves as a compact molecular prior that conditions downstream generative modeling.

Causal MeanFlow. At higher scales, token maps expand rapidly; many positions become trivially predictable from earlier steps, inducing redundancy that over-smooths attention and erodes morphological fidelity (Guo et al., 2025). Moreover, conventional autoregressive models lack causal grounding, resulting in spurious correlations and weakened transcriptomic conditioning. To overcome these limitations, we propose Causal MeanFlow (r-$\mathcal{CM}$), an RNA-conditioned module that enforces causality and preserves gene-driven guidance across scales.

a.) RNA-conditioned Average Velocity Modeling. Departing from classical flow matching based on instantaneous velocity v, we adopt an average-velocity formulation, inspired by Geng et al. (2025), where u is defined as the displacement between two time steps normalized by their interval. This design reduces multi-step integration to a single step, while the instantaneous velocity v can be derived from the interpolated latent $\mathbf{f}_k^t$ at time t and a noise sample ϵ_k, expressed as:

$$\begin{aligned} \mathbf{f}_k^t &= t\mathbf{f}_k + (1-t)\epsilon_k,\ \epsilon_k \sim \mathcal{N}(0,1), \\ v(\mathbf{f}_k^t, t) &= \frac{d(\mathbf{f}_k^t)}{dt} = \mathbf{f}_k - \epsilon_k. \end{aligned} \tag{4}$$

By exploiting the correlation between the average velocity u and the instantaneous velocity v, differentiation with respect to t yields a closed-form expression for u:

$$(t-r)u(\mathbf{f}_k^t, \mathbf{r}_k, \mathbf{z}, t, r) = \int_r^t v(\mathbf{f}_k^\tau, \tau)\, d\tau, \tag{5}$$

$$u(\mathbf{f}_k^t, \mathbf{r}_k, \mathbf{z}, t, r) = v(\mathbf{f}_k^t, t) - (t-r)(v(\mathbf{f}_k^t, t)\partial_{\mathbf{f}_k} u + \partial_t u). \tag{6}$$

We then employ a network Φ, to estimate u conditioned on $\mathbf{z}$ and $\mathbf{r}_k$, with the target average velocity u_{tgt} expressed as:

$$\begin{aligned} u_{\text{tgt}} &= v(\mathbf{f}_k^t, t) - (t-r)(v(\mathbf{f}_k^t, t)\partial_{\mathbf{f}_k} u_\phi + \partial_t u_\phi), \\ \text{where} \quad u_\phi &= \Phi(\mathbf{f}_k^t, \mathbf{r}_k, \mathbf{z}, t, r). \end{aligned} \tag{7}$$

Our network Φ extends beyond Geng et al. (2025) by coupling semantic features from $\mathbf{r}_k$ with transcriptomic signals from $\mathbf{z}$ in the prediction process. This fusion is implemented via biology-enhanced adaptive layer normalization block (adaLN) (Peebles & Xie, 2023), enabling position-wise integration of semantic and biological cues. The procedure is expressed as follows.

$$\begin{aligned} \alpha_1, \beta_1, \gamma_1 = \mathbf{mlp}(\mathbf{z} + t + r);\ \alpha_2, \beta_2, \gamma_2 = \mathbf{mlp}(\mathbf{r}_k + t + r), \\ \tilde{\mathbf{f}} = \mathbf{f}_k^t + \mathbf{attn}(\beta_1 \odot \mathrm{LN}(\mathbf{f}_k^t) + \gamma_1) \odot \alpha_1, \\ \dot{\mathbf{f}} = \mathbf{mlp}(\beta_2 \odot \mathrm{LN}(\tilde{\mathbf{f}} + \mathbf{cattn}(\tilde{\mathbf{f}}, \mathbf{r}_k)) + \gamma_2) \odot \alpha_2, \end{aligned} \tag{8}$$

where $\dot{\mathbf{f}}$ and $\tilde{\mathbf{f}}$ denote intermediate features in r-$\mathcal{CM}$, $\odot$ is the Hadamard product, and "attn," "cattn," and "LN" correspond to attention, cross-attention, and layer normalization, respectively. At inference, r-$\mathcal{CM}$ performs one-step sampling to reconstruct $\hat{\mathbf{f}}_k$ from the scale-aligned embedding $\mathbf{r}_k$:

$$\hat{\mathbf{f}}_k = \epsilon_k - \Phi(\epsilon_k, \mathbf{r}_k, \mathbf{z}, 1, 0),\ \epsilon_k \sim \mathcal{N}(0, 1). \tag{9}$$

b.) Counterfactual Regularization. Autoregressive modeling can be viewed as an iterative reconstruction of quantized features, producing latent representations $\{\mathbf{f}_k^{'}\}_{k=1}^K$. Within our framework, $\mathbf{f}_k^{'}$ is reconstructed from $\mathbf{r}_k$ under the guidance of gene embedding $\mathbf{z}$, progressively enriching semantics across scales. To prevent spurious enhancements from non-causal factors such as color, contrast, or local frequency (Macenko et al., 2009; Tellez et al., 2019; Leek et al., 2010; Aran et al., 2015), we introduce a causal regularization strategy based on counterfactual interventions. Following the principle that interventions must destruct non-causal cues (Zhang et al., 2025), we apply three perturbations—color anomaly (to model stain variation), contrast adjustment (to capture batch effects and scanner differences), and sharpening (to simulate high-frequency artifacts) to generate counterfactual variants X^a, X^c, X^s for each WSI tile X. After quantization, these yield feature maps $\{\mathbf{f}_k^a, \mathbf{f}_k^c, \mathbf{f}_k^s\}_{k=1}^K$, which force Φ to emphasize causal, scale-invariant morphology.

To endow r-$\mathcal{CM}$ with causal regularization, we enlarge the discrepancy between the predicted average velocity u_ϕ and the target velocities $\{u_{\text{tgt}}^a, u_{\text{tgt}}^c, u_{\text{tgt}}^s\}$ obtained from degraded counterfactuals, thereby stabilizing reconstruction. For example, u_{tgt}^a is not derived via costly partial derivatives in Eq. 8. Instead, we decompose average velocity into magnitude and direction, where the direction is computed by normalizing the flow between two sampled fields $\mathbf{f}_k^{a,t}$ and $\mathbf{f}_k^{a,r}$, and the magnitude is estimated by scaling $||u_{\text{tgt}}||$ with a stochastic factor λ. Targets $\{u_{\text{tgt}}^c, u_{\text{tgt}}^s\}$ are constructed analogously. The procedure is formally expressed as:

$$u_{\text{tgt}}^a = \lambda_a ||u_{\text{tgt}}|| \cdot \frac{\mathbf{f}_k^{a,t} - \mathbf{f}_k^{a,r}}{||\mathbf{f}_k^{a,t} - \mathbf{f}_k^{a,r}||}. \tag{10}$$

c.) Learning Objective. We further define a causality-driven learning objective to disentangle scale-invariant morphological semantics (causal factors) from degradation-related cues (non-causal factors). For the k-th iteration, u_{tgt} from $\mathbf{f}_k$ serves as the anchor, while $\mathbf{f}_{k-1}$ is treated as an extreme counterfactual, yielding u_{tgt}^l via Eq. 10. Additional degradation samples $\{u_{\text{tgt}}^a, u_{\text{tgt}}^c, u_{\text{tgt}}^s\}$ derived from independent WSIs, distinct from the source of u_{tgt}, forming the counterfactual set $\mathcal{C}_u$. This design blocks potential shortcuts that exploit non-causal signals and enforces reliance on scale-invariant morphology. The training objective is:

$$\mathcal{L}_\Phi = \mathbb{E}\big[||u_\phi - \mathrm{sg}(u_{\text{tgt}})||^2\big] - \frac{\alpha}{N} \sum_{u_{\text{tgt}}^n \sim \mathcal{C}_u} \mathbb{E}\big[||u_\phi - \mathrm{sg}(u_{\text{tgt}}^n)||^2\big], \tag{11}$$

where $\mathrm{sg}(\cdot)$ denotes stop-gradient and α controls the strength of causal regularization.

RNA-Guided Masked Autoregression. We formulate GeneAR as an autoregressive model over tokenized sequences:

$$p(s_1, s_2, \cdots, s_K) = \prod_{k=1}^{K} p(s_k | s_{<k}, s_0 = \mathbf{z}), \tag{12}$$

Table 1: **Quantitative comparison on TCGA benchmarks.** Fréchet Inception Distance (**FID, lower is better**) is reported along with model parameters (#Para) and generation steps (#Step). GeneAR consistently achieves the best performance across all cohorts.

Type	Method	#Para	#Step	GBM	CESC	KIRP	COAD	LUAD	ALL
Diff.	RNA-CDM (Carrillo-Perez et al., 2025)	1146M	2000	24.15	25.76	24.46	33.60	27.98	23.36
	PathLDM (Yellapragada et al., 2024)	400M	50	22.46	19.87	20.39	26.96	21.28	20.29
	U-ViT (Bao et al., 2023)	297M	100	13.89	15.74	21.83	26.75	17.86	18.55
	DiT (Peebles & Xie, 2023)	305M	250	15.03	18.75	21.53	29.13	18.57	18.11
FM	SiT (Ma et al., 2024)	305M	25	14.63	19.48	22.10	29.47	19.52	18.84
AR	LlamaGen (Sun et al., 2024)	343M	256	15.48	18.34	19.89	27.91	17.52	17.43
	VQGAN (Esser et al., 2021)	227M	256	21.74	23.48	26.10	32.47	26.48	25.09
VAR	VAR (Tian et al., 2024)	310M	10	12.96	17.21	17.32	25.84	15.40	16.83
	ImageFolder (Li et al., 2025)	314M	10	23.75	23.97	25.81	33.25	25.46	24.81
	GeneAR (Ours)	310M	10	**11.24**	**14.17**	**14.99**	**21.02**	**13.70**	**13.66**

This factorization is realized by a ViT-based transformer with a causal mask, ensuring that generation proceeds strictly left-to-right under continuous transcriptomic conditioning, akin to GPT-2.

a.) Gradient-Guided Masking. After r-$\mathcal{CM}$ converges, it produces stable reconstructions $\hat{\mathbf{f}}_k$ from $\mathbf{r}_k$ before passing them to the transformer. We define the gradient as the derivative of the MSE loss between $\mathbf{f}_k$ and $\hat{\mathbf{f}}_k$ with respect to $\mathbf{r}_k$, and compute its ℓ_2 norm along the channel dimension:

$$\mathcal{G}_k = \nabla_{\mathbf{r}_k}(\mathbb{E}||\mathbf{f}_k - \hat{\mathbf{f}}_k||^2), \;\; \mathcal{M}_k = \mathbb{I}(\|\mathcal{G}_k\|_2 > \gamma)\,, \;\; \gamma \sim \mathcal{N}(0,1)^{h_k \times w_k}. \tag{13}$$

Here $\mathbb{I}(\cdot)$ denotes the indicator function. Tokens with large gradient responses are deemed RNA-conditioned salient regions, as perturbations there strongly affect reconstruction. These positions are therefore preferentially retained, dynamically injecting transcriptomic cues at the k-th iteration.

b.) Masked Autoregressive Decoding. Following class/text-conditioned VAR models, the latent gene embedding $\mathbf{z}$ is used as the initial condition token $\mathbf{r}_1$. For subsequent steps, tokens at positions with $\mathcal{M}_k = 0$ are replaced by a learnable embedding $\boldsymbol{e}$. The autoregressive generation and cross-entropy training objective are formulated as:

$$\{s_k^{'}\}_{k=1}^{K} = \mathcal{P}_\Theta(\{\mathbf{r}_1, \cdots, \mathcal{M}_k\mathbf{r}_{k-1}, \mathcal{M}_K\mathbf{r}_K\}), \;\; \mathcal{L}_\Theta = \sum_{k=1}^{K} \mathbb{CE}(s_k^{'}, s_k). \tag{14}$$

For efficiency, masking is applied only when $k \geq K_m$, balancing accuracy and cost. Together, these advances endow GeneAR with causality-aware, biologically grounded generation, which we validate in the next section through comprehensive experiments.

4 Experiments

We evaluate GeneAR on five TCGA[1] cohorts following the RNA-CDM protocol (Carrillo-Perez et al., 2025). Each cohort comprises diagnostic WSIs paired with bulk RNA-Seq profiles and covers five cancer types with case counts: lung adenocarcinoma (LUAD, n=520), kidney renal papillary cell carcinoma (KIRP, n=298), colon adenocarcinoma (COAD, n=289), cervical squamous cell carcinoma and endocervical adenocarcinoma (CESC, n=277), and glioblastoma multiforme (GBM, n=212). Following (Li et al., 2021), we extract non-overlapping 256×256 tiles from gigapixel WSIs at 20× magnification; thus each RNA-Seq profile is associated with the set of tiles from its paired WSI. For generative quality, we report Fréchet Inception Distance (FID; 50K samples) (Heusel et al., 2017). For downstream evaluation, we train tile-level and WSI-level classifiers on synthetic tiles and report F1-score, accuracy (ACC), and AUC.

4.1 Main Results

Comparison with State-of-the-Art Methods. We benchmark our GeneAR against nine strong baselines spanning four families—diffusion (Diff.), flow matching (FM), token-wise autoregres-

[1]The Cancer Genome Atlas Program

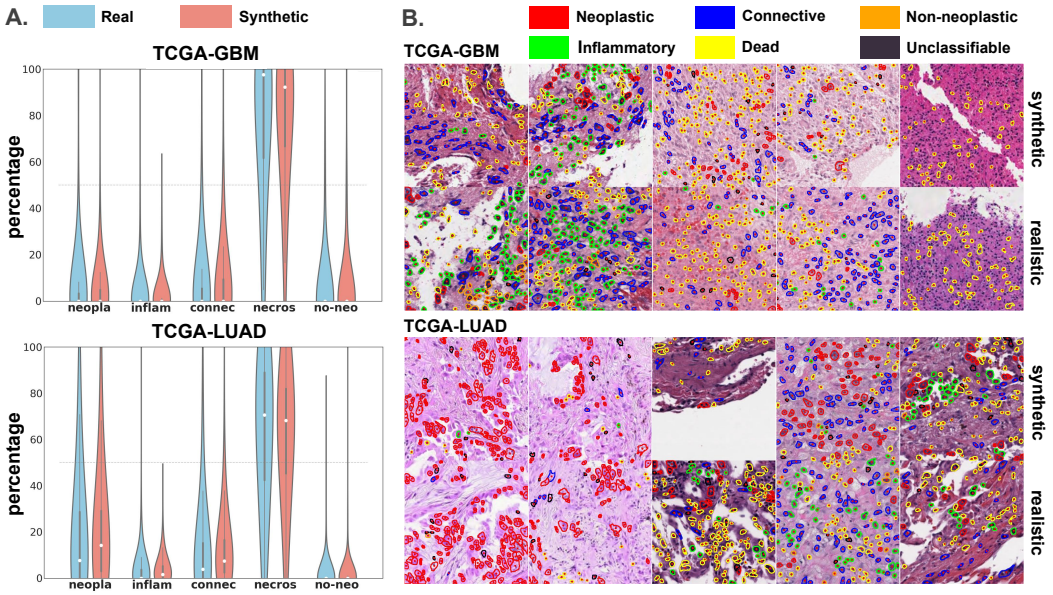

Figure 3: **Synthetic vs. real tiles**. *Panel A.* Cell-type distributions in real and synthetic tiles across TCGA cohorts. *Panel B.* HoverNet (Graham et al., 2019) visualizations showing consistent cellular composition between synthetic and real samples. Best viewed in color.

sion (AR), and scale-wise visual autoregression (VAR). All models are trained on the same cohorts under authors' recommended settings; when a class embedding is required, we replace it with an RNA-Seq embedding layer for parity. We report FID (50K, consisting of average samples spanning all RNA-Seq profiles) per cohort and on the pooled set (ALL). As shown in Tab. 1, our GeneAR achieves record-setting results on all five cohorts: GBM (11.24), CESC (14.17), KIRP (14.99), COAD (21.02), and LUAD (13.70). On the challenging COAD cohort, GeneAR improves over VAR (Tian et al., 2024) by 4.82 FID. Aggregated across cohorts, GeneAR achieves the best overall FID of 13.66 (ALL), outperforming LlamGen (Sun et al., 2024) by 3.77, DiT (Peebles & Xie, 2023) by 4.45, SiT (Ma et al., 2024) by 4.89, and RNA-CDM (Carrillo-Perez et al., 2025) by 9.70.

Table 2: **Cell distribution comparison.** Mean±std of cell proportions across cohorts. Extended results in Tab. 6 (Appendix).

Dataset	Method	Neoplastic	Dead
GBM	VAR	9.96%±21.99	69.55%±34.59
	Ours	**5.04%±12.07**	**78.67%±26.91**
	Real	6.04%±16.29	77.49%±30.90
LUAD	VAR	25.06%±27.38	55.99%±30.00
	Ours	**20.20%±22.78**	**61.10%±26.56**
	Real	19.32%±25.21	63.12%±29.60

Table 3: **Tile classification performance.** ACC/F1 under varying substitution (p) and pretraining (q) ratios. Full results in Tab. 7 (Appendix).

Method	p=0.0		p=0.75	
	ACC	F1	ACC	F1
R-CDM	0.573±0.020	0.556±0.022	0.492±0.016	0.472±0.046
VAR	0.573±0.034	0.556±0.015	0.521±0.030	0.510±0.035
Ours	**0.579±0.032**	**0.570±0.039**	**0.592±0.029**	**0.588±0.031**
	q=0.5		q=1.0	
R-CDM	0.618±0.026	0.612±0.030	0.650±0.021	0.641±0.031
VAR	0.661±0.020	0.662±0.019	0.708±0.011	0.709±0.010
Ours	**0.722±0.023**	**0.722±0.020**	**0.767±0.015**	**0.766±0.017**

Cell Distribution Comparison. While FID captures visual fidelity, biological plausibility is critical for clinical relevance. We therefore evaluate whether synthetic tiles preserve realistic cell composition using HoverNet (Graham et al., 2019), which segments and classifies cells into five categories: neoplastic, inflammatory, connective, dead, and non-neoplastic epithelial. For each benchmark, we randomly sample 2000 tiles from real WSIs and generate equal synthetic counterparts conditioned on RNA-Seq profiles with GeneAR. Quantitative results (Tab. 2) show that cell distributions in our GeneAR closely match real tissues and consistently outperform the strongest baseline VAR (Tian et al., 2024). For example, neoplastic cell proportions are 6.04%±16.29 vs. 5.04%±12.07 in GBM and 19.32%±25.21 vs. 20.20%±22.78 in LUAD. Visual comparisons in Fig. 3 further confirm that GeneAR not only preserves overall cell composition but also generates morphologies consistent with cancer type, demonstrating biological realism beyond mere visual fidelity.

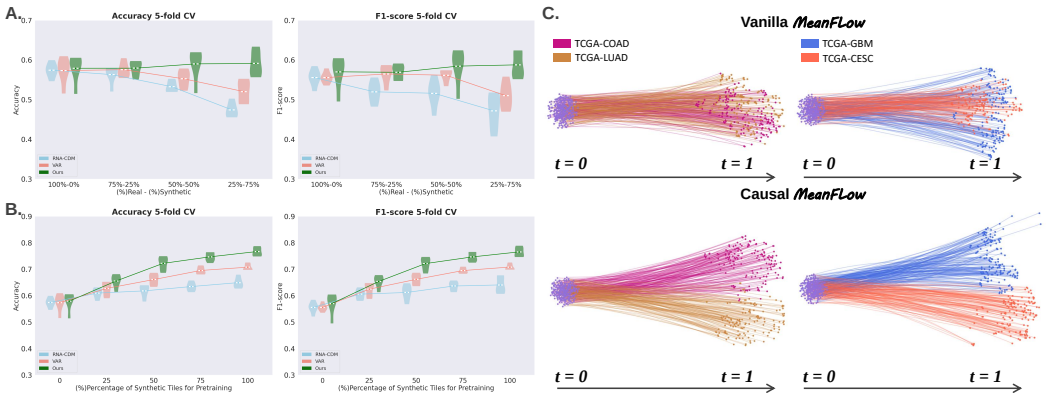

Figure 4: **Classification fidelity and causal dynamics**.*Panel A.* Conventional synthetic tiles degrade classification, whereas GeneAR preserves accuracy. *Panel B.* Pretraining with GeneAR-generated tiles yields the largest performance gains. *Panel C.* Causal MeanFlow disentangles trajectories, revealing class-specific dynamics absent in vanilla MeanFlow. Best viewed in color.

Effect of Causal Regularization. Fig. 4 C illustrates the impact of causal regularization on MeanFlow learning. We employ t-SNE visualization, where points at $t = 0$ denote initial noise and those at $t = 1$ represent one-step generation outcomes; connecting lines approximate the average velocity u. Colors indicate different datasets. For vanilla MeanFlow (Geng et al., 2025), susceptibility to non-causal factors causes substantial overlap of velocity trajectories, reflecting poor class separability. In contrast, our Causal MeanFlow produces clearly separated trajectories, demonstrating its ability to emphasize scale-invariant morphological semantics (causal factors) and capture more fine-grained, class-specific histopathological features.

Tile-Level Validation with Synthetic Data. We used 5,000 model-generated tiles and 5,000 real tiles across five cancer types to evaluate whether synthetic data can sustain classification, employing a ResNet-18 (He et al., 2016) backbone for validation. Substituting up to 75% of real tiles with GeneAR-generated counterparts preserved or slightly improved performance (ACC: 0.579→0.592; F1: 0.570→0.588), whereas RNA-CDM (Carrillo-Perez et al., 2025) and VAR (Tian et al., 2024) caused notable drops (Tab. 3, Fig. 4 A). Pretraining with synthetic tiles further boosted performance, with GeneAR yielding the largest gains (+0.188 ACC, +0.196 F1) and outperforming baselines by clear margins (Tab. 3, Fig. 4 B). These results highlight the clinical utility of GeneAR, showing that model-generated tiles can serve as reliable training data.

WSI-Level Gains with Synthetic Pretraining. Extending to downstream WSI classification under the MIL paradigm, we benchmarked four state-of-the-art methods—TransMIL (Shao et al., 2021), ACMIL (Zhang et al., 2024), WiKG (Li et al., 2024a), and MambaMIL (Yang et al., 2024)—on COAD (MSS vs. MSI). As shown in Tab. 4, synthetic pretraining consistently improved all metrics, with ACMIL achieving the largest gains (ACC +0.096, F1 +0.109, AUC +0.121). These findings demonstrate that GeneAR-generated tiles not only substitute real data effectively but also enable highly discriminative slide-level representations, thereby enhancing downstream clinical classification tasks.

Table 4: **Performance comparison** of MIL methods (w/ vs. w/o pretraining). Our GeneAR generates 512 patch-wise tiles using each RNA-Seq.

Method	ACC		F1-score		AUC	
	w/o	w/	w/o	w/	w/o	w/
TransMIL	0.849	**0.877**	0.847	**0.875**	0.894	**0.934**
ACMIL	0.767	**0.863**	0.749	**0.858**	0.817	**0.938**
WiKG	0.767	**0.822**	0.753	**0.818**	0.820	**0.917**
MambaMIL	0.836	**0.918**	0.833	**0.917**	0.925	**0.941**

4.2 Ablation Study

Analysis of RNA-conditioned Causal MeanFlow. We assess the role of RNA-Seq conditioning and causal inference learning in r-$\mathcal{CM}$ under diverse settings. Reconstruction fidelity is measured by rFID, while FID quantifies overall generative quality within the autoregressive framework. A vanilla $\mathcal{MF}$ directly predicting from $\mathbf{r}_k$ serves as the control. As shown in Tab. 5a, incorporating causal inference learning reduces rFID to 3.70 compared with 4.41 when relying solely on RNA-Seq guidance, but yields a slightly higher FID (15.78 vs. 15.23). This indicates that while causal

Table 5: **Ablation experiments.** We systematically analyze (a) the components of r-$\mathcal{CM}$, (b) RNA-Seq embeddings, (c) core modules of GeneAR, (d) degradation strategies, (e) compatibility with different autoregressive models, and (f) masking strategies.

Settings	rFID (↓)	FID (↓)
Vanilla $\mathcal{MF}$	6.63	16.05
$\mathcal{MF}$ w/ RNA	4.41	15.23
$\mathcal{MF}$ w/ CI	3.70	15.78
r-$\mathcal{CM}$	**2.03**	**13.66**

(a) Key Components of r-$\mathcal{CM}$.

Settings.	FID (↓)
class-label emb.	27.70
linear emb.	22.15
β-VAE	**13.66**

(b) RNA-Seq Embedding.

Settings		FID (↓)
base.(Δ)		16.83
Δ	+ ViT	15.89
	+ $\mathcal{FM}$	14.02
	+ r-$\mathcal{CM}$	**13.66**

(c) Key Components of GeneAR.

u^a_{tgt}	u^c_{tgt}	u^s_{tgt}	rFID (↓)	FID (↓)
✔	✔		2.25	14.36
✔		✔	2.43	14.78
	✔	✔	2.78	15.01
✔	✔	✔	**2.03**	**13.66**

(d) Degradation Methods.

Method	FID (↓)
ImageFloder	24.81
+ r-$\mathcal{CM}$	20.93 (3.88↓)
VAR	16.83
+ r-$\mathcal{CM}$	13.66 (3.17↓)

(e) Compatibility of r-$\mathcal{CM}$.

Settings	FID (↓)
w/o masking	16.83
Random	16.26
E-distance	14.97
Gradient	**13.66**

(f) Masking Strategy.

learning enhances fidelity, RNA-Seq conditioning remains essential for optimal generative quality. Further analysis (Tab. 5d) on counterfactual sample combinations reveals consistent rFID gains of 2.16, 1.98, and 1.63 in rFID across different configurations relative to the baseline (4.41), with FID exhibiting a similar trend. Using all counterfactual variants achieves the lowest rFID and FID, confirming that the full set of degradation strategies is critical for effective causal regularization.

Ablation for Components in GeneAR. We first examine the role of RNA-Seq conditioning (Tab. 5b). Replacing RNA-Seq with class labels leads to a substantial FID degradation of 14.04, highlighting the necessity of biological modulation, while linear embeddings yield moderate improvements but remain 8.49 worse than the β-VAE, reflecting their limited ability to capture complex biological signals. At the model level (Tab. 5c), substituting r-$\mathcal{CM}$ with a non-generative ViT results in a 2.23 FID drop, indicating insufficient capacity to recover fine-grained morphology, whereas flow matching achieves a comparable FID of 14.02 but requires 25$\times$ more steps, underscoring the efficiency advantage of r-$\mathcal{CM}$ in autoregressive modeling.

Compatibility for Visual Autoregressive Modeling. To assess scalability, we integrate r-$\mathcal{CM}$ with gradient-guided masking into two leading visual autoregressive frameworks, VAR (Tian et al., 2024) and ImageFolder (Li et al., 2025). Both benefit substantially, with FID gains of 3.17 for VAR and 3.88 for ImageFolder (Tab. 5e), demonstrating the broad compatibility and effectiveness of our design.

Ablation for Masking Strategy. We compare three masking strategies for selecting causality-enhanced tokens (Tab. 5f). Random masking slightly improves performance (+0.57 over baseline). Euclidean distance-based masking, which prioritizes poorly reconstructed tokens, further reduces FID by 1.86 relative to random masking, but fails to capture causal importance. In contrast, gradient-guided masking achieves the lowest FID of 13.66, outperforming Euclidean masking by 1.31, demonstrating its effectiveness in identifying causally salient tokens and enhancing generation quality.

5 Conclusion

In this work, we introduced GeneAR, an autoregressive Gene-to-WSI tile synthesis model that unites multi-stage transcriptomic conditioning with causality-aware modeling. By reformulating synthesis as an iterative, coarse-to-fine autoregressive process, GeneAR continually reinforces transcriptomic signals, mitigating signal decay and ensuring cross-scale consistency. At its core lies the Causal MeanFlow module, guided by RNA-Seq embeddings, which uses counterfactual interventions to suppress spurious variation and enforce causal fidelity in morphology. Experiments on five TCGA cohorts show that GeneAR achieves state-of-the-art generative fidelity and delivers consistent gains in downstream classification. Beyond benchmarking, GeneAR serves as a controllable tool for probing gene–morphology relationships under transcriptomic perturbations, opening new avenues for integrative studies in computational pathology.

REFERENCES

Dvir Aran, Marina Sirota, and Atul J Butte. Systematic pan-cancer analysis of tumour purity. *Nature Communications*, 2015.

Fan Bao, Shen Nie, Kaiwen Xue, Yue Cao, Chongxuan Li, Hang Su, and Jun Zhu. All are worth words: A vit backbone for diffusion models. In *CVPR*, 2023.

Francisco Carrillo-Perez, Marija Pizurica, Michael G Ozawa, Hannes Vogel, Robert B West, Christina S Kong, Luis Javier Herrera, Jeanne Shen, and Olivier Gevaert. Synthetic whole-slide image tile generation with gene expression profile-infused deep generative models. *Cell Reports Methods*, 2023.

Francisco Carrillo-Perez, Marija Pizurica, Yuanning Zheng, Tarak Nath Nandi, Ravi Madduri, Jeanne Shen, and Olivier Gevaert. Generation of synthetic whole-slide image tiles of tumours from rna-sequencing data via cascaded diffusion models. *Nature Biomedical Engineering*, 2025.

Huiwen Chang, Han Zhang, Lu Jiang, Ce Liu, and William T Freeman. Maskgit: Masked generative image transformer. In *CVPR*, 2022.

Qi Chang, Zhennan Yan, Mu Zhou, Hui Qu, Xiaoxiao He, Han Zhang, Lohendran Baskaran, Subhi Al'Aref, Hongsheng Li, Shaoting Zhang, et al. Mining multi-center heterogeneous medical data with distributed synthetic learning. *Nature communications*, 2023.

Mark Chen, Alec Radford, Rewon Child, Jeffrey Wu, Heewoo Jun, David Luan, and Ilya Sutskever. Generative pretraining from pixels. In *ICML*, 2020.

Weiqing Chen, Pengzhi Zhang, Tu N Tran, Yiwei Xiao, Shengyu Li, Vrutant V Shah, Hao Cheng, Kristopher W Brannan, Keith Youker, Li Lai, et al. A visual–omics foundation model to bridge histopathology with spatial transcriptomics. *Nature Methods*, 2025.

Xinlei Chen, Saining Xie, and Kaiming He. An empirical study of training self-supervised vision transformers. In *ICCV*, 2021.

Youngmin Chung, Ji Hun Ha, Kyeong Chan Im, and Joo Sang Lee. Accurate spatial gene expression prediction by integrating multi-resolution features. In *CVPR*, 2024.

Nicolas Coudray, Paolo Santiago Ocampo, Theodore Sakellaropoulos, Navneet Narula, Matija Snuderl, David Fenyö, Andre L Moreira, Narges Razavian, and Aristotelis Tsirigos. Classification and mutation prediction from non–small cell lung cancer histopathology images using deep learning. *Nature Medicine*, 2018.

Patrick Esser, Robin Rombach, and Bjorn Ommer. Taming transformers for high-resolution image synthesis. In *CVPR*, 2021.

Jevgenij Gamper, Navid Alemi Koohbanani, Ksenija Benes, Simon Graham, Mostafa Jahanifar, Syed Ali Khurram, Ayesha Azam, Katherine Hewitt, and Nasir Rajpoot. Pannuke dataset extension, insights and baselines. *arXiv preprint arXiv:2003.10778*, 2020.

Aniruddha Ganguly, Debolina Chatterjee, Wentao Huang, Jie Zhang, Alisa Yurovsky, Travis Steele Johnson, and Chao Chen. Merge: Multi-faceted hierarchical graph-based gnn for gene expression prediction from whole slide histopathology images. In *CVPR*, 2025.

Yicheng Gao, Kejing Dong, Caihua Shan, Dongsheng Li, and Qi Liu. Causal disentanglement for single-cell representations and controllable counterfactual generation. *Nature Communications*, 2025.

Zhengyang Geng, Mingyang Deng, Xingjian Bai, J Zico Kolter, and Kaiming He. Mean flows for one-step generative modeling. *arXiv*, 2025.

Simon Graham, Quoc Dang Vu, Shan E Ahmed Raza, Ayesha Azam, Yee Wah Tsang, Jin Tae Kwak, and Nasir Rajpoot. Hover-net: Simultaneous segmentation and classification of nuclei in multi-tissue histology images. *Medical image analysis*, 2019.

Hang Guo, Yawei Li, Taolin Zhang, Jiangshan Wang, Tao Dai, Shu-Tao Xia, and Luca Benini. Fastvar: Linear visual autoregressive modeling via cached token pruning. *arXiv*, 2025.

Kaiming He, Xiangyu Zhang, Shaoqing Ren, and Jian Sun. Deep residual learning for image recognition. In *CVPR*, 2016.

Martin Heusel, Hubert Ramsauer, Thomas Unterthiner, Bernhard Nessler, and Sepp Hochreiter. Gans trained by a two time-scale update rule converge to a local nash equilibrium. In *NeurIPS*, 2017.

Irina Higgins, Loic Matthey, Arka Pal, Christopher Burgess, Xavier Glorot, Matthew Botvinick, Shakir Mohamed, and Alexander Lerchner. beta-vae: Learning basic visual concepts with a constrained variational framework. In *ICLR*, 2017.

Jakob Nikolas Kather, Alexander T Pearson, Niels Halama, Dirk Jäger, Jeremias Krause, Sven H Loosen, Alexander Marx, Peter Boor, Frank Tacke, Ulf Peter Neumann, et al. Deep learning can predict microsatellite instability directly from histology in gastrointestinal cancer. *Nature Medicine*, 2019.

Ira Ktena, Olivia Wiles, Isabela Albuquerque, Sylvestre-Alvise Rebuffi, Ryutaro Tanno, Abhijit Guha Roy, Shekoofeh Azizi, Danielle Belgrave, Pushmeet Kohli, Taylan Cemgil, et al. Generative models improve fairness of medical classifiers under distribution shifts. *Nature Medicine*, 2024.

Doyup Lee, Chiheon Kim, Saehoon Kim, Minsu Cho, and Wook-Shin Han. Autoregressive image generation using residual quantization. In *CVPR*, 2022a.

Doyup Lee, Chiheon Kim, Saehoon Kim, Minsu Cho, and WOOK SHIN HAN. Draft-and-revise: Effective image generation with contextual rq-transformer. In *NeurIPS*, 2022b.

Jeffrey T Leek, Robert B Scharpf, Héctor Corrada Bravo, David Simcha, Benjamin Langmead, W Evan Johnson, Donald Geman, Keith Baggerly, and Rafael A Irizarry. Tackling the widespread and critical impact of batch effects in high-throughput data. *Nature Reviews Genetics*, 2010.

Bin Li, Yin Li, and Kevin W Eliceiri. Dual-stream multiple instance learning network for whole slide image classification with self-supervised contrastive learning. In *CVPR*, 2021.

Jiawen Li, Yuxuan Chen, Hongbo Chu, Qiehe Sun, Tian Guan, Anjia Han, and Yonghong He. Dynamic graph representation with knowledge-aware attention for histopathology whole slide image analysis. In *CVPR*, 2024a.

Xiang Li, Kai Qiu, Hao Chen, Jason Kuen, Jiuxiang Gu, Bhiksha Raj, and Zhe Lin. Imagefolder: Autoregressive image generation with folded tokens. *arXiv*, 2024b.

Xiang Li, Kai Qiu, Hao Chen, Jason Kuen, Jiuxiang Gu, Bhiksha Raj, and Zhe Lin. Imagefolder: Autoregressive image generation with folded tokens. In *ICLR*, 2025.

Nanye Ma, Mark Goldstein, Michael S Albergo, Nicholas M Boffi, Eric Vanden-Eijnden, and Saining Xie. Sit: Exploring flow and diffusion-based generative models with scalable interpolant transformers. In *ECCV*, 2024.

Marc Macenko, Marc Niethammer, James S Marron, David Borland, John T Woosley, Xiaojun Guan, Charles Schmitt, and Nancy E Thomas. A method for normalizing histology slides for quantitative analysis. In *ISBI*, 2009.

Maxime Oquab, Timothée Darcet, Théo Moutakanni, Huy Vo, Marc Szafraniec, Vasil Khalidov, Pierre Fernandez, Daniel Haziza, Francisco Massa, Alaaeldin El-Nouby, et al. Dinov2: Learning robust visual features without supervision. *arXiv*, 2023.

William Peebles and Saining Xie. Scalable diffusion models with transformers. In *ICCV*, 2023.

Marija Pizurica, Yuanning Zheng, Francisco Carrillo-Perez, Humaira Noor, Wei Yao, Christian Wohlfart, Antoaneta Vladimirova, Kathleen Marchal, and Olivier Gevaert. Digital profiling of gene expression from histology images with linearized attention. *Nature Communications*, 2024.

Xuyu Qian, Kyle Coleman, Shunzhou Jiang, Andrea J Kriz, Jack H Marciano, Chunyu Luo, Chunhui Cai, Monica Devi Manam, Emre Caglayan, Abbe Lai, et al. Spatial transcriptomics reveals human cortical layer and area specification. *Nature*, 2025.

Ali Razavi, Aaron Van den Oord, and Oriol Vinyals. Generating diverse high-fidelity images with vq-vae-2. In *NeurIPS*, 2019.

Benoît Schmauch, Alberto Romagnoni, Elodie Pronier, Charlie Saillard, Pascale Maillé, Julien Calderaro, Aurélie Kamoun, Meriem Sefta, Sylvain Toldo, Mikhail Zaslavskiy, et al. A deep learning model to predict rna-seq expression of tumours from whole slide images. *Nature Communications*, 2020.

Bernhard Schölkopf, Francesco Locatello, Stefan Bauer, Nan Rosemary Ke, Nal Kalchbrenner, Anirudh Goyal, and Yoshua Bengio. Toward causal representation learning. *Proceedings of the IEEE*, 2021.

Zhuchen Shao, Hao Bian, Yang Chen, Yifeng Wang, Jian Zhang, Xiangyang Ji, et al. Transmil: Transformer based correlated multiple instance learning for whole slide image classification. In *NeurIPS*, 2021.

Peize Sun, Yi Jiang, Shoufa Chen, Shilong Zhang, Bingyue Peng, Ping Luo, and Zehuan Yuan. Autoregressive model beats diffusion: Llama for scalable image generation. *arXiv*, 2024.

David Tellez, Geert Litjens, Péter Bándi, Wouter Bulten, John-Melle Bokhorst, Francesco Ciompi, and Jeroen Van Der Laak. Quantifying the effects of data augmentation and stain color normalization in convolutional neural networks for computational pathology. *Medical Image Analysis*, 2019.

Keyu Tian, Yi Jiang, Zehuan Yuan, Bingyue Peng, and Liwei Wang. Visual autoregressive modeling: Scalable image generation via next-scale prediction. In *NeurIPS*, 2024.

Aaron Van Den Oord, Oriol Vinyals, et al. Neural discrete representation learning. In *NeurIPS*, 2017.

Xiyue Wang, Sen Yang, Jun Zhang, Minghui Wang, Jing Zhang, Wei Yang, Junzhou Huang, and Xiao Han. Transformer-based unsupervised contrastive learning for histopathological image classification. *Medical Image Analysis*, 2022.

Yulun Wu, Louie McConnell, and Claudia Iriondo. Counterfactual generative modeling with variational causal inference. *arXiv*, 2024.

Shu Yang, Yihui Wang, and Hao Chen. Mambamil: Enhancing long sequence modeling with sequence reordering in computational pathology. In *MICCAI*, 2024.

Srikar Yellapragada, Alexandros Graikos, Prateek Prasanna, Tahsin Kurc, Joel Saltz, and Dimitris Samaras. Pathldm: Text conditioned latent diffusion model for histopathology. In *WACV*, 2024.

Lijun Yu, Yong Cheng, Kihyuk Sohn, José Lezama, Han Zhang, Huiwen Chang, Alexander G Hauptmann, Ming-Hsuan Yang, Yuan Hao, Irfan Essa, et al. Magvit: Masked generative video transformer. In *CVPR*, 2023.

Tongshun Zhang, Pingping Liu, Yubing Lu, Mengen Cai, Zijian Zhang, Zhe Zhang, and Qiuzhan Zhou. Cwnet: Causal wavelet network for low-light image enhancement. *arXiv*, 2025.

Yunlong Zhang, Honglin Li, Yunxuan Sun, Sunyi Zheng, Chenglu Zhu, and Lin Yang. Attention-challenging multiple instance learning for whole slide image classification. In *ECCV*, 2024.

A APPENDIX

This appendix provides a comprehensive set of supplementary materials that extend and deepen the contributions presented in the main paper. We begin by revisiting the theoretical underpinnings of MeanFlow, offering a detailed derivation that clarifies its role in modeling average velocity and its integration into GeneAR. Next, we describe the construction of counterfactual samples and the implementation details of training, which together provide greater transparency and reproducibility of our method. Beyond methodology, we report expanded experimental results, including extensive ablation studies, complete quantitative evaluations, and large-scale comparisons with state-of-the-art baselines. Finally, we present supplementary qualitative visualizations that highlight the diversity and realism of the synthesized tiles across multiple cancer types. Taken together, these materials serve to reinforce the rigor of our approach, demonstrate its robustness across varied conditions, and provide deeper insights into its practical implications.

A.1 FURTHER DERIVATION OF MEANFLOW

MeanFlow (Geng et al., 2025) introduces the concept of an average velocity u, defined as the displacement between two time steps t and r, normalized by their interval. This reformulation reduces the multi-step integration of conventional flow matching to a single-step computation, thereby simplifying the generative process. Given Eq. 5, differentiating both sides with respect to t, we can rearrange this formulation to obtain u,

$$u(\mathbf{f}_k^t, \mathbf{r}_k, \mathbf{z}, t, r) = v(\mathbf{f}_k^t, t) - (t-r)\frac{d}{dt}u(\mathbf{f}_k^t, \mathbf{r}_k, \mathbf{z}, t, r). \tag{15}$$

where $\frac{d}{dt}u(\mathbf{f}_k^t, \mathbf{r}_k, \mathbf{z}, t, r)$ denotes the time derivative.

By further expanding the time derivative $\frac{d}{dt}u$ via the chain rule, u can be explicitly expressed as:

$$\begin{aligned}\frac{d}{dt}u(\mathbf{f}_k^t, \mathbf{r}_k, \mathbf{z}, t, r) = &\underbrace{\frac{d\mathbf{f}_k^t}{dt}}_{v(\mathbf{f}_k^t,t)}\partial_{\mathbf{f}_k}u + \underbrace{\frac{d\mathbf{r}_k}{dt}}_{0}\partial_{\mathbf{r}_k}u + \underbrace{\frac{d\mathbf{z}}{dt}}_{0}\partial_{\mathbf{z}}u + \underbrace{\frac{dt}{dt}}_{1}\partial_t u + \underbrace{\frac{dr}{dt}}_{0}\partial_r u, \\ &= v(\mathbf{f}_k^t, t)\partial_{\mathbf{f}_k}u + \partial_t u.\end{aligned} \tag{16}$$

In conclusion, the total derivative can be written as a Jacobian–vector product (JVP), where $[\partial_{\mathbf{f}_k}u, \partial_{\mathbf{r}_k}u, \partial_{\mathbf{z}}u, \partial_t u, \partial_r u]$ constitutes the Jacobian matrix of $u(\mathbf{f}_k^t, \mathbf{r}_k, \mathbf{z}, t, r)$ along the tangent vector $[v, 0, 0, 1, 0]$. Since the ground-truth function u is inaccessible, we employ a network Φ to approximate it. Specifically, in Eq. 16, u is replaced by u_ϕ learned via Φ, and the target average velocity u_{tgt} is ultimately given by:

$$\begin{aligned}u_{\text{tgt}} &= v(\mathbf{f}_k^t, t) - (t-r)(v(\mathbf{f}_k^t, t)\partial_{\mathbf{f}_k}u_\phi + \partial_t u_\phi), \\ \text{where} \quad u_\phi &= \Phi(\mathbf{f}_k^t, \mathbf{r}_k, \mathbf{z}, t, r).\end{aligned} \tag{17}$$

Here, $\partial_{\mathbf{f}_k}u_\phi$ and $\partial_t u_\phi$ can be efficiently computed using the `jvp` interface in PyTorch. The procedure for training Φ with the target u_{tgt} in Eq. 17 is summarized in Alg. 1.

A.2 COUNTERFACTUAL SAMPLE CONSTRUCTION

Effective interventions should perturb non-causal factors while preserving causal content, thereby enabling meaningful causal inference. To this end, we empirically apply three interventions to the ground-truth tiles to construct counterfactual samples, as illustrated in Fig. 5.

Color Anomaly. Following CWNet (Zhang et al., 2025), we apply a color degradation procedure to the original tile X in order to suppress color disturbances. The degradation is defined as:

$$X^a = \Delta H(X) + \Delta S(X) + \sum_{K\in\{R,G,B\}} \Delta K(X) + \epsilon, \tag{18}$$

where H, S, and K denote the hue, saturation, and RGB channel offsets, respectively.

Algorithm 1 Causal MeanFlow: Training

Note: `jvp` interface in PyTorch returns the function output and $\frac{du}{dt}$.

```
# fn(f_k, r_k, z, t, r): function to predict u
# f_k: gt quantinized feature at k scale
# r_k: token embeddings map at k scale
# z: compact molecular prior from RNA_Seq
# t,r: two sampled timestamps
# Counterfactual batch:
# f_k^l: r_k, f_k^a: color anomaly, f_k^c: contrast, f_k^s: sharpening

N = len([f_k^l, f_k^a, f_k^c, f_k^s])
t, r = sample_t_r()
ϵ = randn_like(f_k)

f_k^t = (1 - t) * f_k + t * ϵ
v_k^t = ϵ - f_k^t

u, du/dt = jvp(fn, (f_k, r_k, z, t, r), (v_k^t, 0, 0, 1, 0))
u_tgt = v_k^t - (t - r) * du/dt
u_tgt_m = ||u_tgt||

for f_k^j in {f_k^l, f_k^a, f_k^c, f_k^s}:
    ϵ_j = randn_like(f_k^j)
    f_k^{j,t} = (1-t) * f_k^j + t * ϵ_j
    f_k^{j,r} = (1-r) * f_k^r + r * ϵ_j
    d_j = f_k^{j,t} - f_k^{j,r}
    norm(d_j) = d_j / ||d_j||
    u_tgt^j = λ_j * u_tgt_m * norm(d_j)

C_u = {u_tgt^l, u_tgt^a, u_tgt^c, u_tgt^s}
error = u - sg(u_tgt)
for u_tgt^n in C_u:
    error_inven += (u - sg(u_tgt^n))

loss = metric(error) - α/N * metric(error_inven)
```

Contrast Adjustment. To prevent spurious semantic enhancement caused by contrast variation, we introduce a contrast adjustment intervention:

$$X^c = \sum_{K\in\{R,G,B\}} \Big[\alpha_K \cdot (X_K - \mu_K) + \mu_K\Big] + \epsilon, \tag{19}$$

where α_K and μ_K are the contrast coefficient and channel-wise mean of the K-th channel.

Sharpening Operation. Similarly, to mitigate spurious semantic enhancement introduced by local spatial frequency distributions, we design a sharpening intervention:

$$X^s = X + \alpha \cdot (X - \text{Blur}(X)) \cdot k, \tag{20}$$

where α and k control the sharpening intensity and lightness coefficient, respectively, and $\text{Blur}(\cdot)$ denotes Gaussian blurring.

A.3 Implementation Details

MSVQ $\mathcal{Q}$. All scales share a unified codebook $\mathcal{V} \in \mathbb{R}^{4096\times 32}$, comprising 4096 entries of 32-dimensional vectors, with the number of discrete token maps per image fixed at $K = 10$. A DINOv2-based encoder (Oquab et al., 2023) is used to obtain continuous latent representations, followed by a decoder that reconstructs images from the quantized *token maps*. Subsequently, we

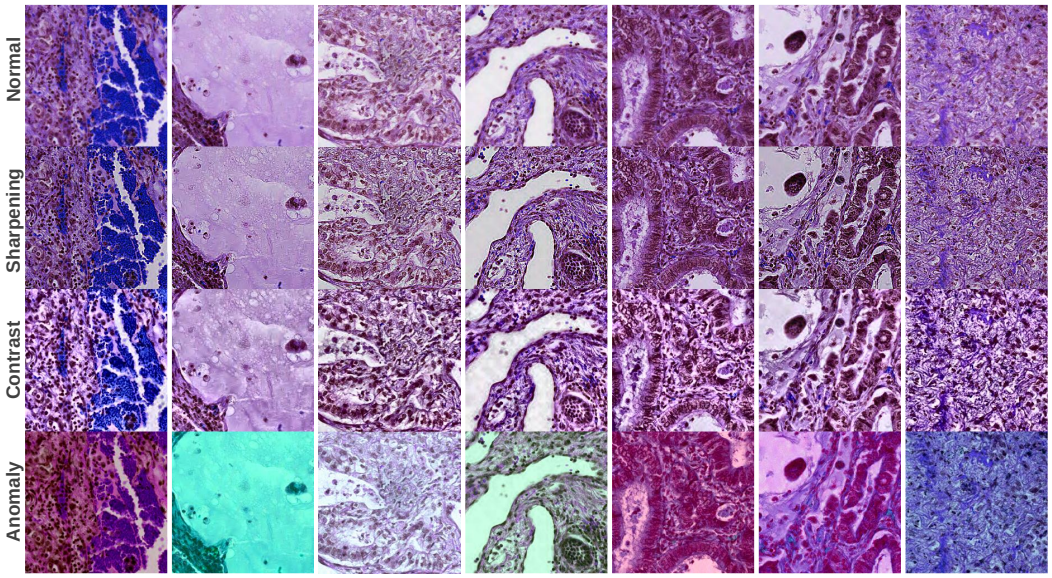

Figure 5: **Visualizations of counterfactual samples**. Our degradation procedures perturb non-causal factors while maintaining the morphology information.

randomly sample approximately 31 tiles per WSI associated with each RNA-Seq profile, constructing a total of 50,000 tiles, yielding an rFID of 2.11.

Causal MeanFlow. r-$\mathcal{CM}$ adopts the SiT architecture (Peebles & Xie, 2023) for the network Φ, with model depth and feature dimension set to 6 and 768, respectively. The hyperparameter α is fixed at 0.1, and λ is uniformly sampled from $[0.8, 1.2]$. r-$\mathcal{CM}_\Phi$ is trained for 100 epochs using 50 tiles per WSI. Additionally, we randomly sample approximately 31 tiles per WSI associated with each RNA-Seq profile, yielding a total of 50,000 tiles for rFID evaluation in Tab. 5a and Tab. 5d.

RNA-Guided Masked Autoregression. The VAR transformer follows the standard architecture with depth $d = 16$, head count $h = d$, and width $w = 64h$. Training is performed using an AdamW optimizer with initial learning rate 10^{-4}, batch size 256, $\beta_1 = 0.9$, $\beta_2 = 0.95$, and weight decay 0.05. After pretraining r-$\mathcal{CM}$, we freeze its parameters and integrate it into the training of $\mathcal{P}_\Theta$ for 200 epochs using 200 tiles per WSI. The MSVQ module $\mathcal{Q}$ is trained jointly on the same tile sampling protocol.

Code Availability. The implementation of GeneAR, including training scripts and pretrained models, will be made publicly available upon publication.

A.4 Extended Experimental Results

Comprehensive Cell Distribution Comparison. Tab. 6 reports the complete cell distributions of five cell types across five datasets, provided as a supplement to Tab. 2. For each dataset, we synthesize 2,000 tiles using all RNA-Seq profiles and randomly sample 2,000 real tiles. HoverNet (Graham et al., 2019), trained on the PanNuke dataset (Gamper et al., 2020), is employed to detect neoplastic, inflammatory, connective, dead, and non-neoplastic cell types. For each dataset, cell distributions are first quantified at the tile level, and then aggregated to obtain overall statistics across the 2,000 tiles. The results demonstrate that synthetic tiles generated by GeneAR better capture realistic cell-type distributions and further improve the morphological fidelity of synthesized tissue. Representative visualizations are provided in Fig. 6.

Comprehensive Tile Classification Analysis. Comprehensive results under different proportions p and q are reported in Tab. 7. For GeneAR, classification accuracy does not decline even as the fraction of synthetic tiles steadily increases within the 5000 mixed tiles, whereas all competing methods exhibit significant performance degradation. Moreover, classification accuracy continues to improve with the progressive incorporation of synthetic tiles during pretraining. Notably, GeneAR

Table 6: **Comparison of various cell distributions.** We systematically analyze the distributions of cell populations at the tile level across five cancer types, reporting both the mean and standard deviation (mean±std) of the corresponding cell proportion.

Dataset	Method	Neoplastic	Inflammatory	Connective	Dead	Non-Neoplastic
GBM	VAR	9.96% ± 21.99	1.64% ± 5.46	15.87% ± 26.84	69.55% ± 34.59	2.95% ± 12.01
	Ours	5.04% ± 12.07	2.80% ± 7.60	8.97% ± 17.15	78.67% ± 26.91	4.49% ± 12.70
	Real	6.04% ± 16.29	2.82% ± 8.86	8.39% ± 19.19	77.49% ± 30.90	5.24% ± 16.06
CESC	VAR	30.92% ± 31.89	1.44% ± 5.20	19.04% ± 26.68	47.47% ± 32.18	1.10% ± 6.53
	Ours	27.19% ± 24.82	2.05% ± 5.52	13.31% ± 19.57	56.67% ± 26.64	0.77% ± 3.21
	Real	25.67% ± 28.43	2.73% ± 9.43	12.21% ± 21.66	58.77% ± 30.56	0.60% ± 2.95
LUAD	VAR	25.06% ± 27.38	2.99% ± 6.84	15.23% ± 20.63	55.99% ± 30.00	0.71% ± 3.42
	Ours	20.20% ± 22.78	3.95% ± 5.86	13.16% ± 15.14	61.10% ± 26.56	1.56% ± 6.64
	Real	19.32% ± 25.21	3.57% ± 6.86	12.46% ± 19.40	63.12% ± 29.60	1.52% ± 7.04
KIRP	VAR	20.59% ± 25.29	3.52% ± 8.01	9.22% ± 18.70	60.78% ± 26.97	2.72% ± 8.30
	Ours	22.61% ± 23.44	2.91% ± 4.64	9.36% ± 13.89	63.32% ± 25.53	1.78% ± 4.76
	Real	23.07% ± 26.71	2.44% ± 5.78	8.04% ± 16.01	64.43% ± 29.85	2.00% ± 7.23
COAD	VAR	33.37% ± 33.08	2.01% ± 7.29	27.39% ± 28.00	36.08% ± 29.55	1.13% ± 6.71
	Ours	38.14% ± 28.25	2.81% ± 5.00	20.09% ± 20.19	38.25% ± 24.69	0.69% ± 2.37
	Real	35.54% ± 32.95	3.32% ± 7.77	19.87% ± 24.85	40.49% ± 29.66	0.76% ± 3.45

Table 7: **Tile classification performance** under different substitution ratios p of real tiles with synthetic ones, and varying proportions q of synthetic tiles used for pretraining. Four different proportions for the pretraining 25% (1,250 samples), 50% (2,500 samples), 75% (3,750 samples) and 100% (5,000 samples). All experiments are conducted under a 5-fold cross-validation (CV) protocol to guarantee the stability and reliability of the results.

Method	p=0.0		p=0.25		p=0.50		p=0.75	
	ACC	F1-score	ACC	F1-score	ACC	F1-score	ACC	F1-score
RNA-CDM	0.573 ± 0.020	0.556 ± 0.022	0.563 ± 0.024	0.520 ± 0.028	0.533 ± 0.014	0.516 ± 0.036	0.492 ± 0.016	0.472 ± 0.046
VAR	0.573 ± 0.034	0.556 ± 0.015	0.576 ± 0.020	0.565 ± 0.026	0.553 ± 0.022	0.561 ± 0.017	0.521 ± 0.030	0.510 ± 0.035
Ours	**0.579 ± 0.032**	**0.570 ± 0.039**	**0.580 ± 0.020**	**0.569 ± 0.020**	**0.590 ± 0.037**	**0.585 ± 0.042**	**0.592 ± 0.029**	**0.588 ± 0.031**
	q=25%		q=50%		q=75%		q=100%	
RNA-CDM	0.612 ± 0.021	0.606 ± 0.020	0.618 ± 0.026	0.612 ± 0.030	0.635 ± 0.017	0.637 ± 0.018	0.650 ± 0.021	0.641 ± 0.031
VAR	0.628 ± 0.025	0.625 ± 0.024	0.661 ± 0.020	0.662 ± 0.019	0.695 ± 0.013	0.698 ± 0.010	0.708 ± 0.011	0.709 ± 0.010
Ours	**0.656 ± 0.023**	**0.654 ± 0.022**	**0.722 ± 0.023**	**0.722 ± 0.020**	**0.747 ± 0.016**	**0.747 ± 0.015**	**0.767 ± 0.015**	**0.766 ± 0.017**

achieves larger gains than the two SOTA baselines. Classification models are trained for 50 epochs, with each pretraining stage fixed at 20 epochs.

Comprehensive WSI Classification Analysis. WSI classification follows the standard multi-instance learning framework, where all tiles extracted from an individual WSI form a tile-wise bag associated with a slide-level label: 0 for microsatellite stability (MSS) and 1 for microsatellite instability (MSI). Tile features are first extracted by a designated feature extractor and then fed into a classification model to predict the slide-level label. To assess the clinical utility of synthetic tiles, we adopt two tile feature extractors—ViT (Chen et al., 2021) pre-trained with MoCoV3 and CTransPath (Wang et al., 2022) pre-trained with SRCL—together with four state-of-the-art WSI classification models. We evaluate on the COAD MSI dataset (Kather et al., 2019), which includes 298 MSS and 66 MSI slides from 360 patients. Specifically, 292 slides for training and 72 slides for testing. For each RNA-Seq profile, GeneAR generates 512 synthetic tiles to construct tile-wise bags for classifier pretraining. As shown in Tab. 8, all classifiers consistently achieve significant gains across both feature extractors.

Table 8: **Performance comparison of MIL methods** with and without pretraining across four SOTA models. Shaded cells indicate results with pretraining.

Method	ACC		F1-score		AUC	
	w/o	w/	w/o	w/	w/o	w/
ViT pre-trained with MoCo V3						
TransMIL	0.849	0.877	0.847	0.875	0.894	0.934
ACMIL	0.767	0.863	0.749	0.858	0.817	0.938
WiKG	0.767	0.822	0.753	0.818	0.820	0.917
MambaMIL	0.836	0.918	0.833	0.917	0.925	0.941
CTransPath pre-trained with SRCL						
TransMIL	0.822	0.849	0.821	0.843	0.862	0.900
ACMIL	0.808	0.849	0.800	0.847	0.836	0.936
WiKG	0.767	0.836	0.745	0.829	0.876	0.912
MambaMIL	0.781	0.849	0.766	0.844	0.867	0.912

Table 9: **Ablation on the injection timing of r-$\mathcal{CM}$.** "Time" denotes the relative training time per epoch, while "Inject." indicates the number of r-$\mathcal{CM}$ injection operations. Shaded cell indicates the best FID.

K_m	FID ↓	Time	Inject.
7	14.39	1.51×	4
8	13.52	1.30×	3
9	13.66	1.00×	2
10	15.74	0.86×	1

A.5 Additional Ablation Results

Ablation for K_m. Injecting r-$\mathcal{CM}$ at every autoregressive step incurs considerable computational redundancy. To address this, we analyze token maps across scales $\{1, 2, 3, 4, 5, 6, 8, 10, 13, 16\}$ and find that the final two token maps account for 62.5% of the total sequence length (680). Based on this observation, the initial value of K_m is empirically set to 9. We then evaluate GeneAR under a range of K_m values. As reported in Tab. 9, setting $K_m = 8$ yields only a marginal improvement in FID (0.14) but comes at the cost of a 1.30× increase in per-epoch training time compared to $K_m = 9$.

A.6 Supplementary Visualization Results

To further illustrate the generative capacity of GeneAR, we provide additional qualitative results in Fig. 7. These synthetic H&E-stained tiles are generated across five representative cancer types (GBM, CESC, LUAD, KIRP, and COAD). The examples demonstrate that GeneAR is capable of producing diverse histological patterns that remain visually realistic while preserving disease-specific morphology. Such results highlight the robustness of GeneAR in synthesizing tissue structures that are consistent with biological priors, thereby complementing the quantitative evaluations reported in the main paper.

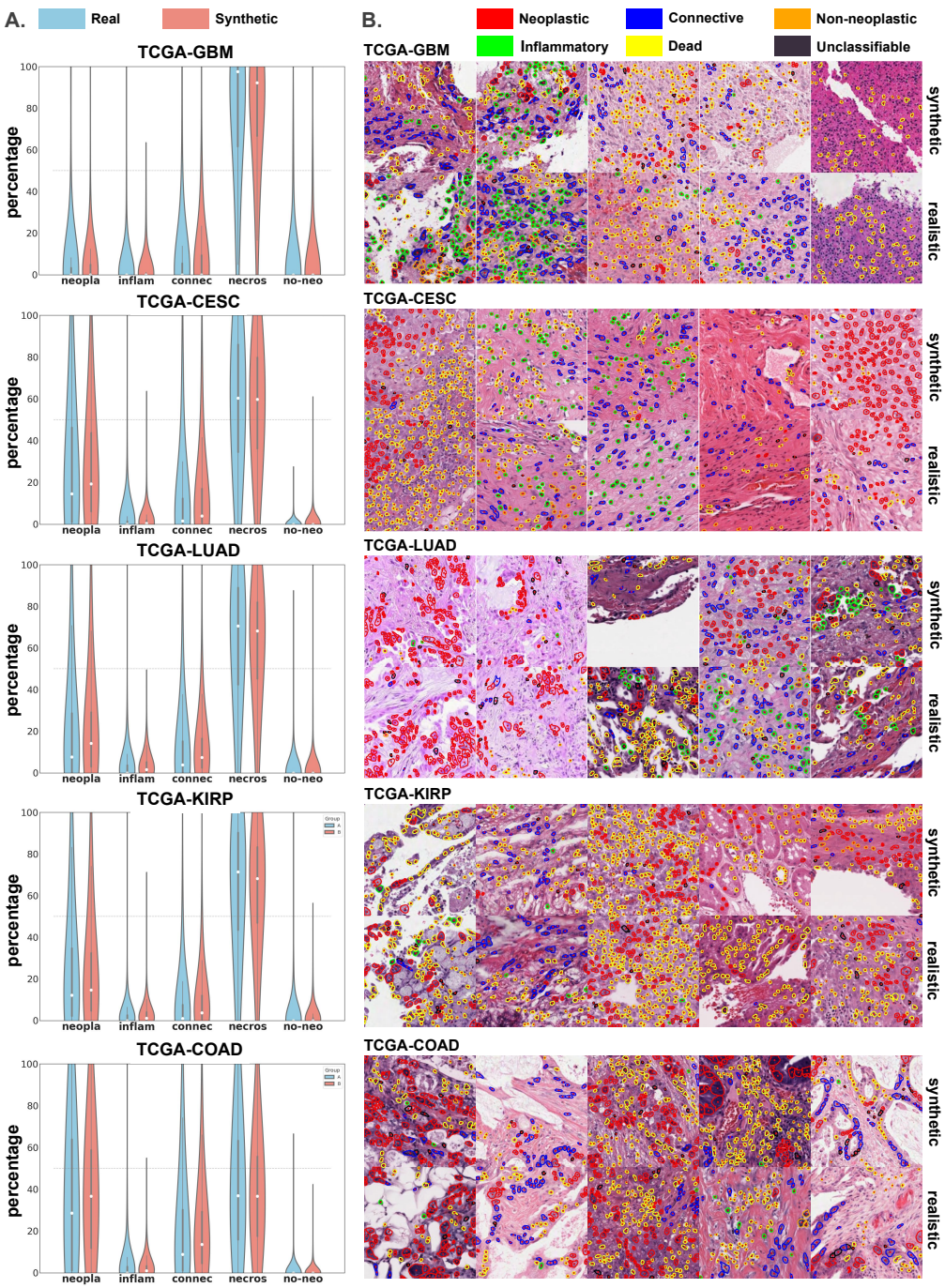

Figure 6: **Panel A.** Comparison of cell-type distributions between synthetic and real tiles across five cancer types. **Panel B.** Visualization of cells detected by HoverNet (Graham et al., 2019), showing neoplastic, inflammatory, connective, dead, and non-neoplastic populations in both synthetic and real samples.

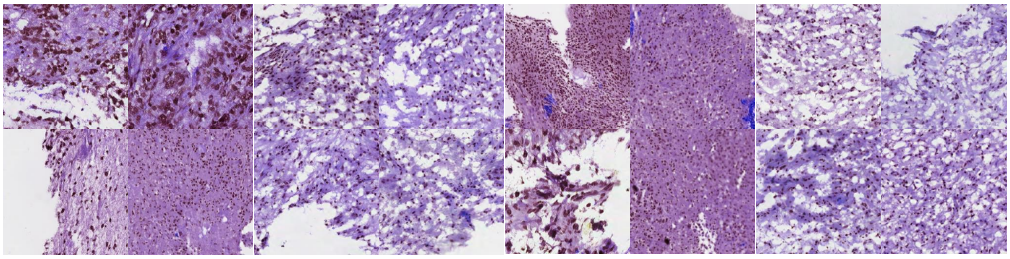

(a) Synthetic H&E-stained WSI tiles from GeneAR for GBM.

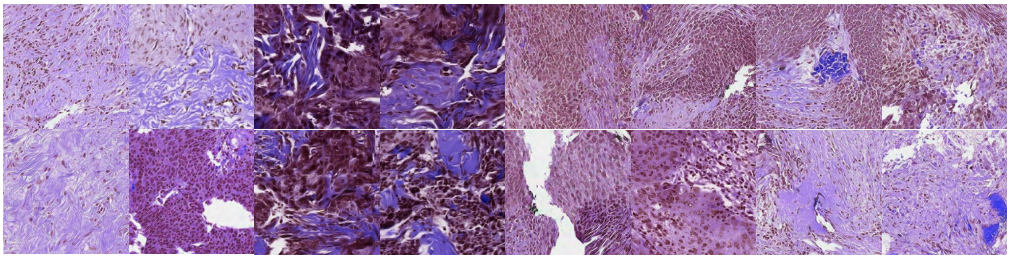

(b) Synthetic H&E-stained WSI tiles from GeneAR for CESC.

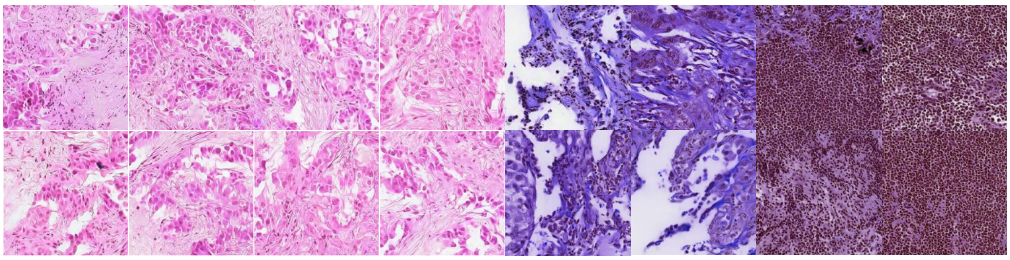

(c) Synthetic H&E-stained WSI tiles from GeneAR for LUAD.

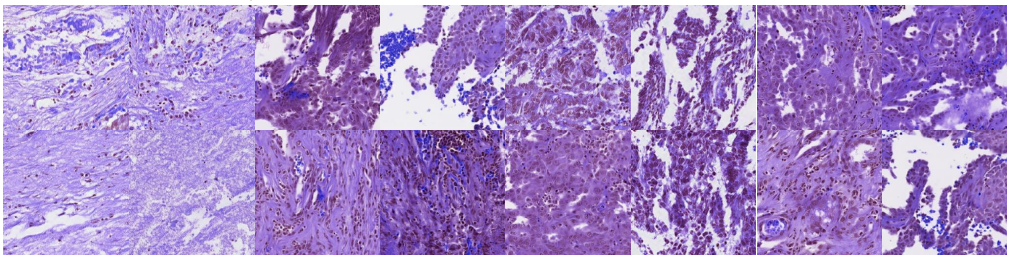

(d) Synthetic H&E-stained WSI tiles from GeneAR for KIRP.

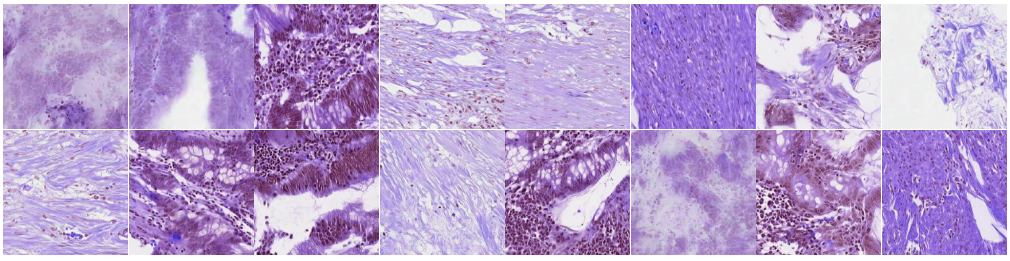

(e) Synthetic H&E-stained WSI tiles from GeneAR for COAD.

Figure 7: **Synthetic H&E-stained WSI tiles** generated by GeneAR across five cancer types: (a) GBM, (b) CESC, (c) LUAD, (d) KIRP, and (e) COAD. The results demonstrate that GeneAR can synthesize diverse and realistic histological patterns.